Cz-Silicon Produced from Solar Grade and Recycled Materials. Part I: Bulk Properties and Formation of As-Grown Defects

SONG ZHANG, EIVIND JOHANNES ØVRELID, MARI JUEL, and GABRIELLA TRANELL

The current paper is the first of two, investigating the properties of Czochralski-silicon (Cz-silicon) materials and solar cells produced with recycled and compensated silicon materials. In this work, impurity levels in two experimental Cz-silicon ingots were characterized by glow discharge mass spectroscopy and FTIR. The combined effects of these impurities on recombination properties were investigated by photoluminescence imaging and compared to bulk properties of a reference ingot. Ring pattern distribution of as-grown micro-defects in the ingots, related to elevated carbon and oxygen levels, were delineated based on the results of two steps of dry oxidation. Moreover, the mechanism of defect formation in the experimental Cz-Si during solidification and oxidation is elaborated in light of thermodynamic theories. Meanwhile, the positive effect of phosphorus in compensated feedstock is discussed in relation to the minority carrier lifetime based on the quasi-steady-state photoconductance results, as well as on the restricted formation of oxygen-related defects during solidification by analyzing samples after oxidation and copper decoration.

DOI: 10.1007/s40553-014-0038-1
© ASM International (ASM) and The Minerals, Metals, & Materials Society (TMS) 2014

I. INTRODUCTION

THE relationship between the type and density of crystal defects and the presence of impurities has been receiving considerable attention in the last few years as it has been observed that the existence of grown-in micro-defects (GMDs) in Czochralski-silicon (Cz-Si)[1–6] leads to the formation of highly efficient recmbinant centers and decreases the performance of solar cells.[7,8] A number of works on the structure and formation mechanism of the GMDs have been published in the last decades,[9–13] and all investigations show their dependence on the interstitial oxygen, which is one of the main impurities in Cz-silicon. Meanwhile, the development of new metallurgical refining and recycling technologies provides alternative feedstock for the PV industry.[14] Given these developments, the formation mechanisms of GMDs become more complex and dependent on the combination of impurities present in any given material. To date, however, there have been no systematic studies with respect to the concentration of GMDs generated in Cz ingots made from recycled or combinations of the recycled and metallurgically produced feedstock materials, *i.e.*, concurrent effect of higher concentrations of light elements (C, N, O) and sometimes higher concentrations of metallic impurities. Such investigations are important to improve the knowledge of the opportunities and limitations of alternative feedstock in Cz-silicon and associated solar cells.

In this paper, we report on the concurrent effects of light elements (oxygen and carbon), dopants, and metallic impurities on the formation of defects as well as the possible mechanisms behind their formation in Cz-Silicon pulled from recycled and compensated feedstock. Studies of the GMDs have been carried out with optical and photoluminescence methods. Based on the results, the interrelation between bulk recombination properties and GMDs was established.

II. EXPERIMENTAL MATERIALS AND METHODS

A. *Feedstock*

In this work, two experimental feedstocks as well as standard poly-silicon were used to produce Cz-silicon in a puller (PVA Tepla model EKZ2700). One of the experimental feedstocks was the standard, metallurgically produced Elkem Solar Silicon (ESS),[15] the other recycled top cut (~upper 50 mm) of p-type multicrystalline ingot.

Figure 1(a) shows an image from a near-infrared camera (NIR) which was used to illustrate the impurities in the recycled feedstock under a halogen lamp illumination. As revealed by the image, the feedstock contains both particles and needles. After dissolution of the silicon in Chemical Polishing 4 (CP4) etchant solution ($HF + HNO_3 + CH_3OOH$, typical ratio 3:5:3 solution), the presence of needles and particles was demonstrated to relate to carbon and nitrogen, displayed in Fig-

SONG ZHANG, Research Scientist, and GABRIELLA TRANELL, Associate Professor, are with the Department of Materials Science and Engineering, Norwegian University of Science and Technology (NTNU), 7491 Trondheim, Norway. Contact e-mail: songz@material.ntnu.no EIVIND JOHANNES ØVRELID, Associate Professor, and MARI JUEL, Research Scientist, are with the SINTEF Materials and Chemistry, 7491 Trondheim, Norway.
Manuscript submitted July 1, 2014.
Article published online November 21, 2014

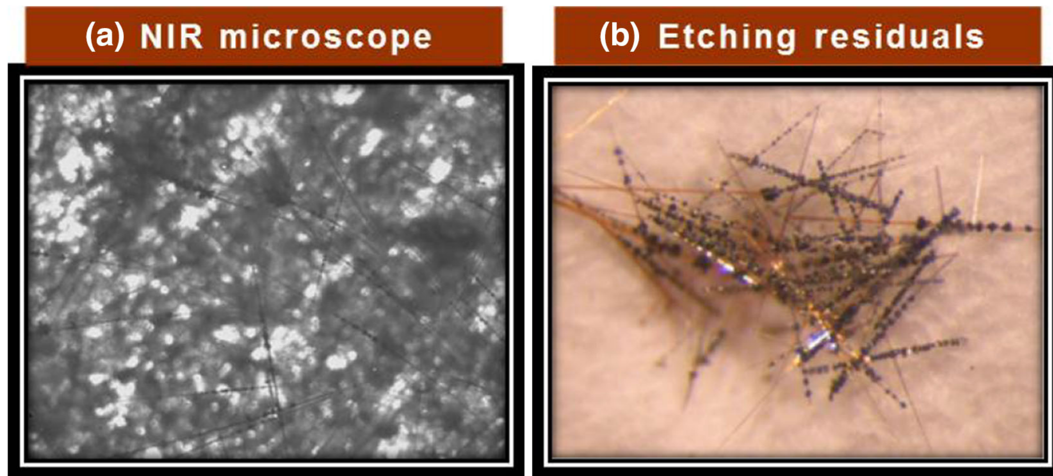

Fig. 1—Purity characterization of recycled materials. (*a*) Infrared micrograph; (*b*) particles extracted from silicon top cut (15 mm upper cut by etching away the silicon). Needles are silicon nitrides, particles are silicon carbides (~50 mm distance from the top cut of standard p-type multi-crystal ingot made from poly/silicon).

ure 1(b)). Prior to pulling, the recycled materials were treated through low energy consumption process developed by Norwegian Si Pro AS, which mainly consists of water-based and surface abrasion cleaning procedures, besides the removal of highly contaminated areas.

B. *Cz Pulling*

Ingot Cz1 was pulled from a 50/50 (pct) mixture of recycled material and standard ESS material, while the second ingot, Cz2, was pulled from 100 pct recycled top cut material. The two experimental ingots and a third, standard poly-silicon reference ingot (RS), were grown under identical pulling conditions as listed in Table I.

No process problem or apparent structure loss occurred during pulling of either of the experimental ingots. As illustrated in Figure 2, the body parts were separated from the ingot top and bottom according to the industrial standard cutting scheme to avoid the transfer region from interstitials to vacancies, *i.e.*, approximately 25 mm below shoulder edge and 50 mm above tail edge in this work. The selected body is approximately 200-mm diameter and 1480-mm length, respectively.

C. *Sample Preparation*

All ingots were cut to 156 mm × 156 mm quasi-square in radial direction, and then divided in seven blocks from 50 mm below the seed end to 50 mm above the bottom marked with S1-B#-T1, as shown in Figure 2. The properties of these blocks were characterized *via* analysis of two kinds of wafer, 156 mm × 156 mm × 2000 mm (Slab1 (S1)-Slab7 (S7)) and 156 mm × 156 mm × 200 μm (W1-W12), respectively. Five extra wafers were selected as test samples from the top to tail blocks to evaluate the stability throughout both ingots. Four point probe (FPPs) method for resistivity measurement was performed on slabs after rapid thermal processing to eliminate the detrimental effect of oxygen thermal donors which usually increase resistivity in p-type silicon. Glow

Table I. List of Pulling and Size Parameter

Ingot #	Pulling Rate (mm)	Diameter (mm)	Yields (kg)
Cz 1	~1.1	~203	110
Cz 2	~1.1	~204	113
RS	~1.1	~203	114

discharge mass spectrometry (GDMS)[16] was carried out on central parts of these slabs (S1-S7) to reveal the metallic impurity concentrations. Interstitial oxygen [O_i] and substitutional carbon [C_s] concentrations were measured by Fourier transform infrared spectroscopy (FTIR) at room temperature (where the optical absorption lines of O_i and C_s are at 1107 and 605 cm^{-1}, respectively), which were quantified according to ASTM F118-93a[17] and ASTM F1391-93[18] standards.

D. *Lifetime Measurement*

All samples were mechanically polished and then chemically polished to assure a uniform surface and reproducible area. After polishing, the samples were then cleaned in RCA1 (NH_4OH(28 pct):H_2O_2(30 pct):CH_3COOH(100 pct) = 1:1:5 in volume) and RCA2 (NH_4OH(28 pct):HCL(27 pct):CH_3COOH(100 pct) = 1:1:6 in volume) at 348.15 K (75 °C) to eliminate the organic and metallic contamination, the last step being an HF (5 pct) rinse followed by a deionized water rinse. Double surface passivation with amorphous silicon was performed in a PECVD chamber to reveal bulk recombination properties of experimental wafers through PL. quasi-steady-state photoconductance (QSSPC) was used to characterize the minority carrier lifetime of the samples.

E. *Oxidation and Copper Decoration*

The GMDs were revealed in terms of extended defects introduced *via* copper decoration and oxidation processing steps. Copper decoration was performed by

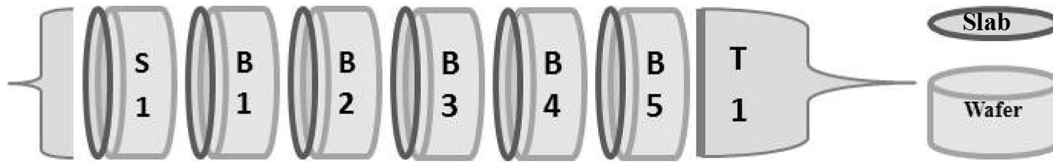

Fig. 2—Cutting scheme of experimental ingots.

Table II. Metallic Impurities Concentration as Determined by Glow Discharge Mass Spectrometry (GDMS)

	Dopant (ppbw)			Light Elements (ppma)		Metallic Impurities (ppbw)		
Samples #	B	P	Resistivity ρ (Ω cm)	O_i	C_s	Fe	Cu	Al
Cz1 body top (S)	140	215	~1.45	23.9	2	4	150	21
Cz1 body tail (T)	210	410	~1.45	12.3	7	7.2	220	30
Cz2 body top (S)	100	—	1.4	26.3	2	1.2	89	11.8
Cz2 body tail (T)	170	—	0.8	14.2	11.2	20	220	21
RS body top (S)	52	—	3.2	20.8	<1	1.1	60	18
RS body tail (T)	80	—	1.8	11.8	~1	6	75	19

spreading 3 mol/L $Cu(NO_3)_2$ solution on the back surface of each sample, baking on a hot plate at elevated temperature to dry the solution for 2 hours and subsequently heating the samples in a muffle furnace at 1173.15 K (900 °C) for 30 minutes, followed by cooling in air [room temperature 293.15 K (20 °C)]. The oxidation process was based on Semi standard two-step annealing,[19] *i.e.*, moderate temperature [1323.15 K (1050 °C)] for 16 hours in oxygen and nitrogen atmosphere after low temperature pre-treatment [1023.15 K (750 °C)] for 4 hours.

F. *Preferential Etching*

A critical ratio (1:2) of oxidant ($K_2Cr_2O_7$) to dissolving agent (HF), known as Secco etching, was used to delineate micro-defects distribution in the experimental samples after specified heat treatments. Specified by this etching solvent, the related D-defects are well known as flow pattern defects (FPDs) based on their shape under microscope.[20]

III. RESULTS AND DISCUSSION

The samples used in the study were selected from the top and bottom of the effective yield of Cz Si ingots according to industrial standards, which can be approximately referenced for estimation in the following PV application. Table II shows the sample parameters which were measured by GDMS, FTIR, and Four Point Probes (FPPs). With the exception of Cu, Cz1 and Cz2 do not show significantly higher levels of metallic impurities compared to RS; the B doping levels are significantly higher in Cz 1 and 2 compared to RS; Cz1 also provides a higher level of P compared to both Cz2 and RS. Typically, low resistivity throughout the experimental ingots is due to high doping level, and smooth values illustrate that there is no transfer from p- to n-type at the Cz1 body bottom.

In addition to differences in doping levels, the concentration of light elements (O_i and C_s) in Cz1 and Cz2 is significantly higher compared with the samples from RS. Toward the top part of both the Cz 1 and 2 ingots, [O_i] almost reaches super-saturation levels which easily give rise to O_i-related micro-defects, and precipitates. Moreover, the level of [O_i] is also slightly higher in Cz2 as compared to Cz1, which gives us an opportunity to compare the effects of higher oxygen levels in combination with high [P] and [C_s]. Based on the earlier characterization of the top cut material, we conclude that the higher [C_s] originates from feedstock rather than the pulling process, as opposed to the elevated [O_i] level, which is greatly affected by the Cz pulling process even under apparently identical process parameters.

A. *Defects-Related Recombination*

PL- and micro-defect-related characterizations were used to delineate the distribution and types of the defects. Figure 3 shows PL image of wafers from the Cz1, Cz2, and RS ingots, respectively, after amorphous silicon passivation, a method proven to reduce the surface recombination velocity to <10 cm/s.[21] The weak PL signal at the edges is an effect of insufficient passivation in those areas. In contrast to the standard RS wafers, there are distinct dark areas with ring patterns on wafers of Cz1 and Cz2. Moreover, the ring pattern defect distribution on Cz1 and Cz2 wafers differs significantly. The obvious rings on Cz1 wafers are fewer and weaker and only observed in a short range below the seed end, like Cz1-S image displayed in Figure 3. Inversely, the ring defects on Cz2 wafers were still visible on the bottom sample at nearly 80 pct solid fraction of the body and seemed much more complex than Cz1. Based on the observations from our previous investigation of Cz-silicon with high carbon levels, the ring patterns are coupled to the significant light element concentrations ([O_i] and [C_s]) as listed in Table II.

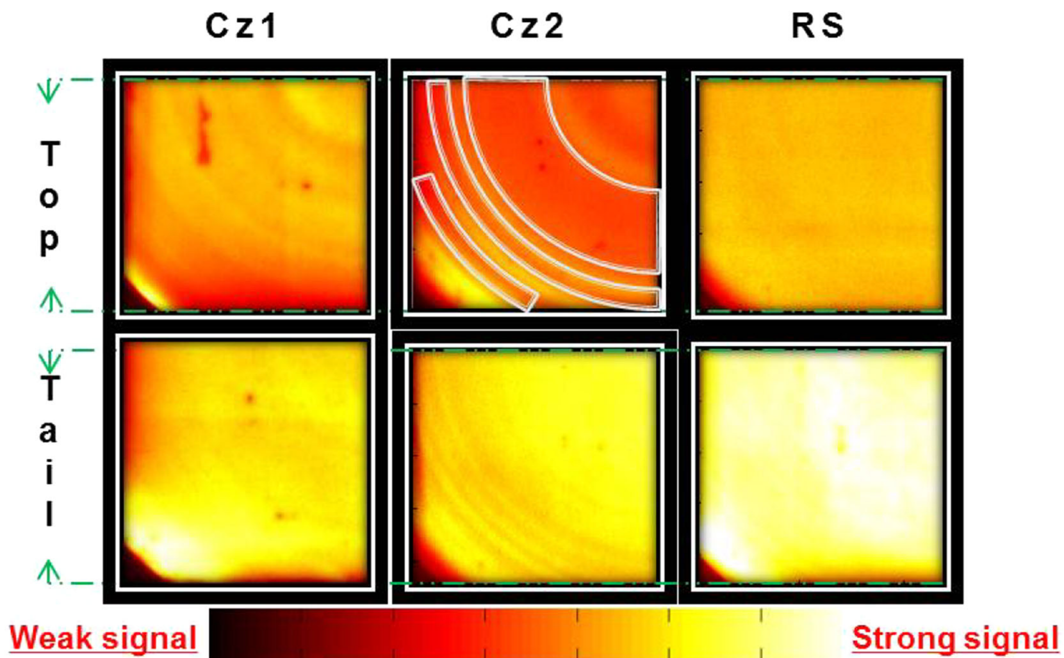

Fig. 3—PL images of wafers in samples of Cz1, Cz2, and RS, all wafers passivated with a-Si.

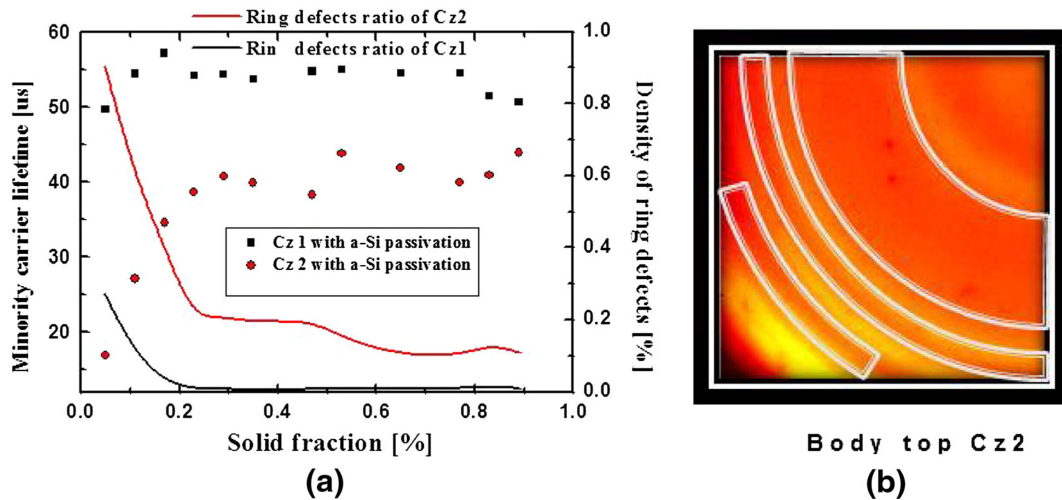

Fig. 4—Minority carrier lifetime of experimental samples passivated with a-Si. (*a*) Correlation of minority carrier lifetime of wafers along ingots to the ring pattern defect strength, (*b*) Cz2 body top wafer taken as an example for calculation of the ring defects density.

Isovalent carbon introduces more vacancies into the silicon lattice by trapping the interstitial silicon during crystallization.[22] Residual vacancies combine with oxygen to form activated recombination centers, as ring patterns. Along with the growth of the ingots, the recombination properties were limited by decreasing $[O_i]$ even at higher $[C_s]$ levels. The mechanisms of ring pattern formation will be discussed in more detail below.

QSSPC analysis performed on the same batch of wafers (200 μm) with the same surface passivation as the reference (RS) wafers reveals the bulk properties at different positions along the ingot in longitudinal direction. It can be seen that the lifetimes of Cz1 are generally higher than those of Cz2. This should be attributed to the slightly lower doping level or the compensation effect according to MacDonald.[23] The minority carrier lifetime increases with the increasing solid fraction in Cz2, while it is relatively constant and higher throughout Cz1 as compared to Cz2, as shown in Figure 4(a). In order to find out if the differences in lifetime are correlated with the intensity of the rings visible in the PL images, we set up a simple metric *i.e.*, the density of ring patterns $\alpha = A_{\mathrm{ring}}/A_{\mathrm{w}}$, where A_{ring} is the area of ring patterns with weak signal shown in Figure 4(b); A_{w} is the area of the whole wafer. Following this metric, the lifetime related to ring defect strength is plotted on the right-hand axis in Figure 4(a). The trends of the minority carrier lifetime *vs* the density of ring patterns from the analysis displayed in Figure 4(a) illustrate that the gradual improvement of electrical performance is correlated with more homogeneous signals on the PL images, *i.e.*, lower ring pattern

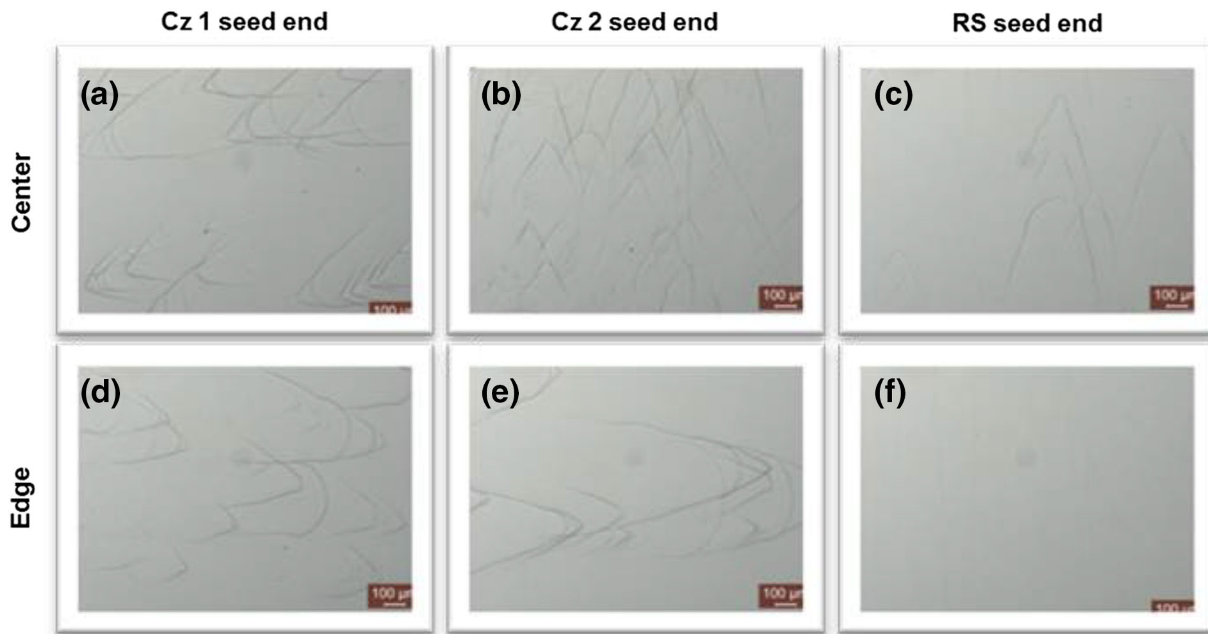

Fig. 5—FPDs' density on the seed end samples (*a*) through (*c*) are center parts, while (*d*) through (*f*) are edge parts.

strength gave rise to a higher minority carrier lifetime in both the Cz1 and Cz2 ingots. Considering the complex impurity combination (metallic and light elements impurities) throughout ingots originating from the recycled feedstock, more in-depth analysis of defects to account for the formation and effects of ring patterns as high recombination areas is required.

B. *Flow Pattern Defects*

Figure 5 shows optical microscopy photographs of bulk FPDs after Secco etching for each sample taken from the seed end of experimental and reference ingots. A large amount of FPDs displayed on the surface illustrate a vacancy model growth during the solidification of the three ingots. It can be seen that the densities of FPDs on the Cz1 and Cz2 are higher than the reference sample in the center or edge regions in radial direction. For all experimental samples, the appearance of FPDs at the sample edge region was likely induced by the higher vacancy concentration introduced by elevated carbon levels rather than other contaminants, as evidenced by the annihilated FPDs displayed in the reference samples.

C. *Oxidation*

Figure 6 shows oxidation results taken from triangle samples of the Cz1 and Cz2 body top after two-stage annealing [1023.15 K (750 °C) 4 hours + 1323.15 K (1050 °C) 16 hours] and preferential etching (Secco etching).[24] By this procedure, incorporated interstitial oxygen [O_i] experienced a super-saturated state and nucleated preferentially at efficient sites of increased surface potential such as surface and crystal defects. White contrast ring patterns were revealed in radial direction after this procedure, as shown in Figures 6(a) and (b). Optical microscopy pictures show areas which were selected adjacent to the star marks on the etched surfaces of the Cz1 and Cz2 body top samples. A high density of etching pits can be seen on the surfaces of the both samples, shown as stick and point-like shapes in Figures 6(c) through (f). Based on Semi MF 1809-0704[25] and Voronkov's theories,[12] the stick-shaped precipitates correspond to extrinsic oxygen stacking faults (EOSFs) which were aggregated around GMDs with critical size such as oxygen particles and clusters, while smaller but higher density precipitates formed nearby as-grown point defects with smaller size or other heterogeneous points introduced during the first annealing step. It can be seen that the optical microscopic images of Cz1 show relatively lower density of etching pits especially with stick shape at the center region (Pos. 3) and compared to Cz2 (Pos. 4) in Figure 6. It seems that compensation effect in Cz1 could suppress the formation of stacking faults.

The [O_i] difference tested *via* FTIR displayed in Figure 7(a), before and after annealing, is the evidence of the effect of oxygen precipitation during annealing processes. As discussed above, the density of EOSFs formed during two-step annealing should be proportional to the density of correlated GMDs. In order to determine the influence of GMDs on the as-grown bulk properties, the densities of EOSFs in Cz1 and Cz2 seed end samples are plotted *vs* the camera signals of PL images (from Figure 3), respectively, as shown in Figure 7(b). These data were selected from representative positions, including ring pattern region, center part, and edge of both samples, respectively. As predicted, an approximate linear relationship between the PL signals of passivated samples and EOSFs rather than the total oxygen precipitates are revealed in both samples. It can

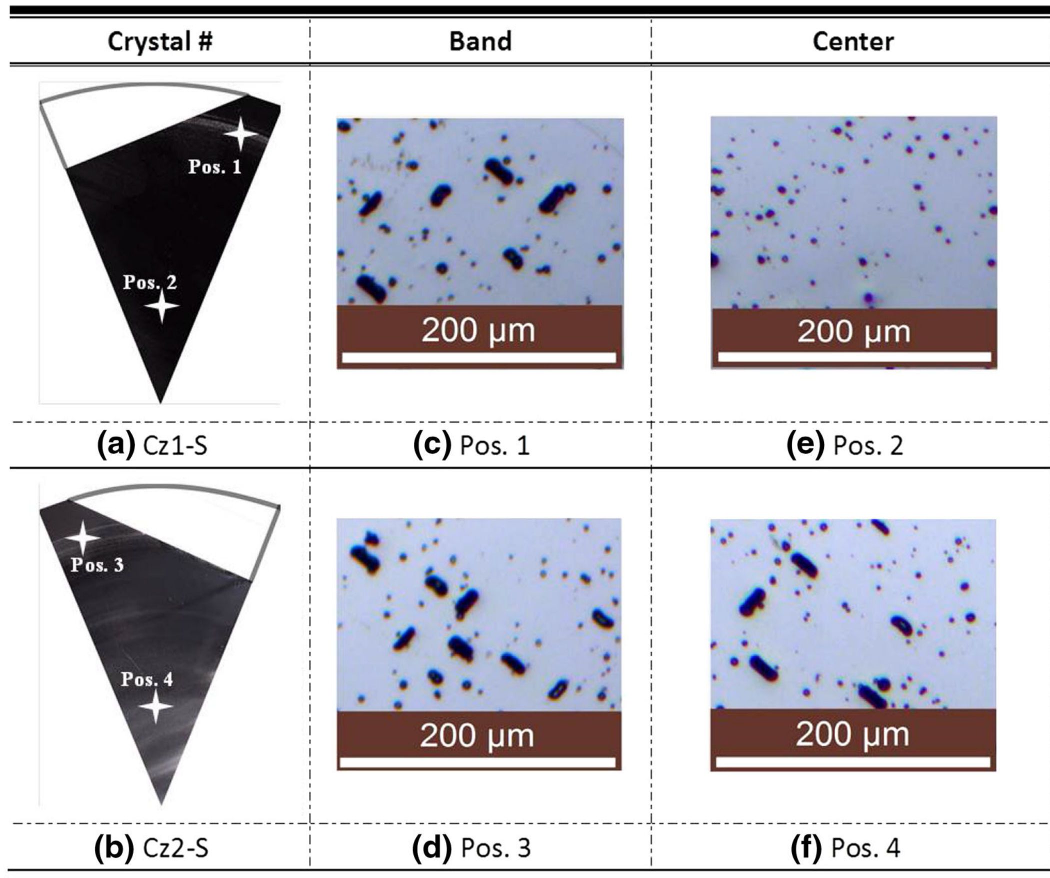

Fig. 6—Preferential etching surface on oxidized Cz1 and Cz2 triangle body top wafers; (*a*) and (*b*) Photographs after preferential etching, (*c*) through (*f*) Optical microscopy pictures taken from representative positions nearby the marks Pos. 1, 2, 3, and 4 on the Cz1 and Cz2 body top samples.

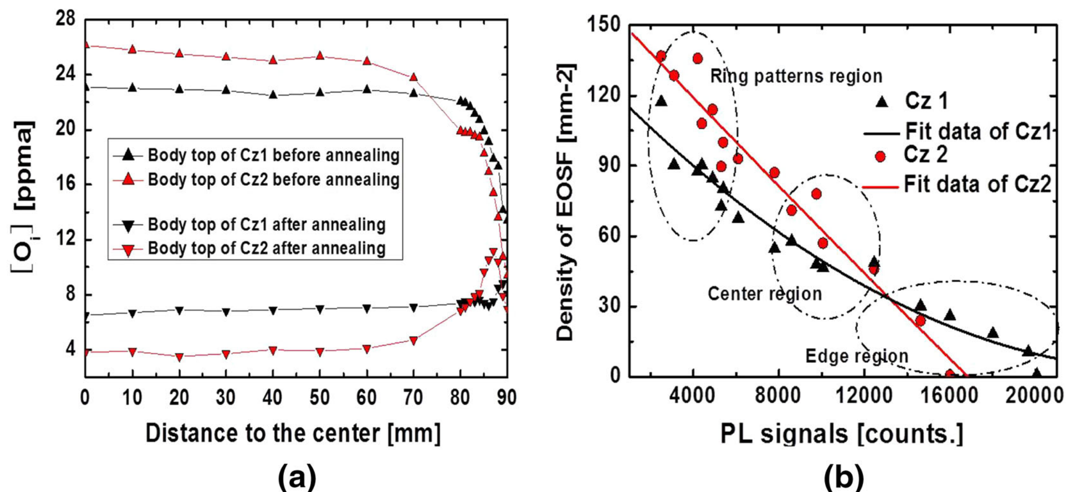

Fig. 7—Influence of annealing processes on the bulk properties. (*a*) Interstitial oxygen concentration and (*b*) density of external stacking faults after annealing processes along the radius direction on the wafers.

be seen that the PL signals are inversely proportional to the density of EOSFs. We therefore conclude that the GMDs as the nuclei for EOSFs during two-step annealing are the main cause of the ring pattern distribution of the minority carrier lifetime in our samples, as shown in Figure 3. Our previous research[26] has illustrated that the presence of considerable [C_s] could suppress the formation of as-grown defects correlated to EOSFs after oxidation. Therefore, it is reasonable to believe that the presence of carbon in our

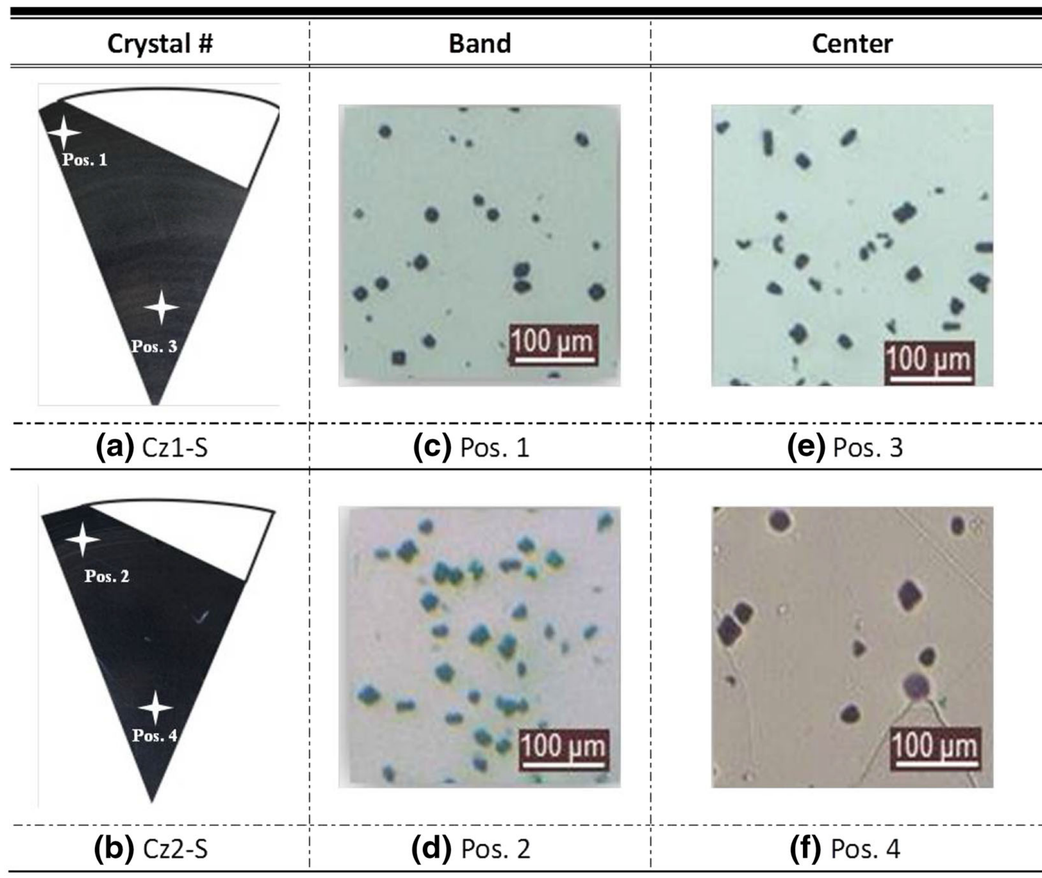

Fig. 8—Photography and optical microscopy pictures of Cu-decorated samples after secco etching under bright light.

experimental samples could reduce the impact of oxygen-related defects on the minority carrier lifetime.

Fewer defect regions near the edge of the samples were likely due to two facts: (a) no effective nuclei, *i.e.*, size of grown-in defects < critical size, which act as the core during moderate temperature processing due to the consumption of vacancies *via* recombination and out-diffusion; (b) they are interstitial regions which could inhibit the formation of precipitates.[27]

D. *Copper Decoration*

Further evidence of a large amount of grown-in defects in our experimental ingots was revealed through copper decoration. Figure 8 shows photographs of a Cu-decorated wafer after preferential etching work, taken under bright light. From optical microscopy images of four selected positions (marked as Pos. 1 to 4), high densities of copper precipitates were displayed. A ring pattern distribution in the horizontal direction from the center to the facet, similar to the above oxidation discussion, is apparent. However, slightly different and even inverse results can be observed between the copper precipitates and oxidation results. The Cz1 sample displayed a higher density of copper deposition inside the band nearby the edge (Pos. 1 and Pos. 2) than that in Cz2, as shown by the comparison between Pos. 3 and Pos. 4 in Figure 8. Previous research[28] has indicated the structure of copper precipitates as orthorhombic η''-Cu_3Si. The unit volume of this kind of precipitate is more than that of silicon. As such, the continuous aggregation and growth of the precipitates would eject Si and need to release compressive stress by incorporating available vacancies in addition to efficient nuclei.[29] Therefore, a high concentration of copper precipitates is likely due to a higher residual vacancy concentration or other ways to overcome the inner compression, such as isovalent C_s, which usually introduces tensile stress into the silicon lattice. The slightly lower copper precipitate concentration in Cz2 compared to Cz1 at the center regions could thus be explained by more vacancies being consumed during solidification to form as-grown micro-defects such as oxygen particles and even oxygen precipitates which correspond to the EOSFs after oxidation, considering relatively higher [O_i] and similar [C_s] in both samples (see Table II).[9]

Another proposed reason for the different densities of copper precipitates is the presence of phosphorous in Cz1 compared to Cz2. The availability of phosphorous in Cz1, facilitating the formation of phosphorus-vacancy complexes[30] appears to depress the formation of high density and large size oxygen-related particles by combining the vacancies during solidification. These complexes were not stable at the copper decoration temperature 1173.15 K (900 °C),[31] and thus become active, providing extra vacancies during copper deposi-

tion to release the compressive stress. Inversely, the higher density of oxygen-related defects in Cz2 consumed a great quantity of vacancies during solidification in the temperature range 1273.15 K to 1373.15 K (1000 °C to 1100 °C).[12,32] As a result, fewer residual vacancies were available during copper decoration processes.

IV. CONCLUSIONS

Two industrial-sized P-type Cz ingots have been pulled -without apparent structure loss- from recycled top cut Si from multi-crystalline ingots, with or without addition of Elkem Solar Silicon (ESS) feedstock. Bulk properties of the resulting ingot materials have been investigated and compared to those of a standard Cz ingot pulled from poly-silicon. The results can be summarized as follows:

1. The experimental ingots both have a higher net compensation level than the reference ingot and hence show lower resistivity. The ingot containing 50 pct ESS feedstock had a lower net doping level than the ingot containing 100 pct recycled feedstock due to a higher concentration of P.
2. Both experimental ingots have significantly higher concentrations of light elements O and C than the reference ingot, while metallic impurities (except for Cu) are at the same level. It shows that Cz technique is more efficient to reduce the metallic impurities than O and C.
3. As-grown micro-defects (GMDs) in the experimental ingots were revealed as oxygen-related defects (voids and oxygen particles, *etc.*). Higher density and complicated types of GMDs as the nuclei for EOSFs during oxidation are typical and determine the ingot bulk properties, distributing in the form of ring patterns. Therefore, isovalent carbon was presumed to properly improve the properties of our experimental samples by suppressing the formation of as-grown defects which mostly grow into the EOSFs after oxidation. As such, bulk properties of experimental ingots are limited by these ring pattern defects, showing more dependence on $[O_i]$ rather than $[C_s]$.
4. The ingot containing ESS™ feedstock with a high level of P has significantly better bulk properties and fewer ring pattern defects than the ingot with 100 pct recycled feedstock. In addition to slightly different $[O_i]$ in Cz1 and Cz2, it is proposed that compensation and P–V complexes are the possible causes for the improved performances of material, *i.e.*, the lower free carriers and vacancy trapped by phosphorus depress the activity and formation of oxygen-related defects.

ACKNOWLEDGMENTS

Use of materials from the Eurostars project—E!6588 RESIM project are gratefully acknowledged. We are grateful to Erik Stensrud Marstein of IFE for kindly supplying the PL instrument used in this study. Thanks are also due to Yu Hu and Chiara Modanese for providing a QSSPC and GDMS data analysis and etching guides.

REFERENCES

1. D.C. Walter, B. Lim, K. Bothe, R. Falster, V.V. Voronkov, and J. Schmidt: *Sol. Energy Mater. Sol. Cells*, 2014, vol. 131, pp. 51–57.
2. T. Xu, X.P. Zhang, X.Y. Ma, and D.R. Yang: *Mater. Sci. Semicond. Process.*, 2013, vol. 16, pp. 893–98.
3. M. Arivanandhan, R. Gotoh, K. Fujiwara, S. Uda, Y. Hayakawaa, and M. Konagaic: *Scripta Mater.*, 2013, vol. 69, pp. 686–89.
4. V.V. Voronkov and R. Falster: *J. Electrochem. Soc.*, 2002, vol. 149 (3), pp. 167–74.
5. V.V. Voronkov and R. Falster: *Mater. Sci. Eng. B*, 2006, vol. 134, pp. 227–32.
6. J.D. Murphy, R.E. McGuire, K. Bothe, V.V. Voronkov, and R.J. Falster: *Sol. Energy Mater. Sol. Cells*, 2014, vol. 120, pp. 402–11.
7. L. Chen, X.G. Yu, and P. Chen: *Sol. Energy Mater. Sol. Cells*, 2011, vol. 95, pp. 3148–51.
8. J. Haunschild, J. Broisch, I.E. Reis, and S. Rein: *26th European Photovoltaic Solar Energy Conference and Exhibition, 5–9 September 2011*, Hamburg, Germany, pp. 1025–30.
9. V.V. Voronkov: *J. Cryst. Growth*, 2008, vol. 310, pp. 1307–14.
10. M. Meduna, O. Caha, and J. Bursık: *J. Cryst. Growth*, 2012, vol. 348, pp. 53–59.
11. T. Abe: *Mater. Sci. Eng. B*, 2000, vol. 73, pp. 16–29.
12. V.V. Voronkov and R. Falster: *J. Cryst. Growth*, 1998, vol. 194, pp. 76–78.
13. T.W. Fan, J.J. Qian, J. Wu, L.Y. Lin, and J. Yuan: *J. Cryst. Growth*, 2000, vol. 213, pp. 276–82.
14. S. Pizzini: *Sol. Energy Mater. Sol. Cells*, 2010, vol. 94, pp. 1528–33.
15. J. Safarian, G. Tranell, and M. Tangstad: *Energy Proc.*, 2012, vol. 20, pp. 88–97.
16. M. Di Sabtino, A.L. Dons, J. Hinrichs, and L. Arnberg: *Spectrochim. Acta B*, 2011, vol. 66 (2), pp. 144–48.
17. ASTM: "Standard Test Method for Interstitial Atomic Oxygen Content of Silicon by Infrared Absorption", 1993.
18. ASTM: "Standard Test Method for Substitutional Atomic Carbon Content of Silicon by Infrared Absorption", 1993.
19. ASTM: "Test Method for Oxygen Precipitation Characteristics of Silicon Wafers by Measurement of Interstitial Oxygen Reduction", 2002.
20. J.F. Zhang and C.C. Liu: *J. Cryst. Growth*, 2004, vol. 269, pp. 310–16.
21. S. Dauwe, J. Schmidt, and R. Hezel: *Proceedings of the 29th IEEE PVSC*, New Orleans, 2002, pp. 1246–49.
22. P. Pichler: in *Intrinsic Point Defects, Impurities and Their Diffusion in Silicon*, S. Selberherr, ed., Springer Verlag, Wien, 2004.
23. D. MacDonald and A. Cuevas: *J. Appl. Phys.*, 2011, vol. 109 (043704), pp. 1–8.
24. D.H. Hwang, S.M. Hur, and K.H. Lee: *J. Cryst. Growth*, 2003, vol. 249, pp. 37–43.
25. ASTM: "Standard Guide for Selection and Use of Etching Solutions to Delineate Structural Defects in Silicon", 2002.
26. S. Zhang, M. Juel, E.J. Øvrelid, and G. Tranell: *J. Cryst. Growth*, Accepted on 28th Oct., 2014.
27. V.V. Voronkov and R. Falster: *J. Appl. Phys.*, 1999, vol. 8 (11), pp. 5975–82.
28. J.K. Solberg: *Acta Crystallogr. Sect. A*, 1978, vol. 34, pp. 684–98.
29. M.S. Kulkarni and J. Libbert: *J. Electrochem. Soc.*, 2002, vol. 149, pp. 153–65.
30. R.Y. Chen, B. Trzynadlowski, and S.T. Dunham: *J. Appl. Phys.*, 2014, vol. 115, pp. 054906-1–6-6.
31. S. Dannefaer, G. SuppCz, and V. Avalos, *J. Phys.*, 2009, vol. 21, pp. 015802-1–2-6.
32. Y.R. Li and N. Imaishi: *J. Cryst. Growth*, 2004, vol. 266, pp. 48–53.